



# Assessing seasonal and interannual water storage variations in Taiwan using geodetic and hydrological data

Ya-Ju Hsu<sup>a,b,\*</sup>, Yuning Fu<sup>c</sup>, Roland Bürgmann<sup>d</sup>, Shao-Yiu Hsu<sup>e</sup>, Chin-Cheng Lin<sup>b</sup>, Chi-Hsien Tang<sup>a,b</sup>, Yih-Min Wu<sup>a,b,f</sup>

<sup>a</sup> Institute of Earth Sciences, Academia Sinica, Taipei, Taiwan

<sup>b</sup> Department of Geosciences, National Taiwan University, Taipei, Taiwan

<sup>c</sup> School of Earth, Environment and Society, Bowling Green State University, Bowling Green, OH, USA

<sup>d</sup> Berkeley Seismological Laboratory, University of California, Berkeley, CA, USA

<sup>e</sup> Department of Bioenvironmental System Engineering, National Taiwan University, Taipei, Taiwan

<sup>f</sup> NTU Research Center for Future Earth, National Taiwan University, Taipei, Taiwan

## ARTICLE INFO

### Article history:

Received 3 March 2020

Received in revised form 23 June 2020

Accepted 14 August 2020

Available online 7 September 2020

Editor: J.P. Avouac

### Keywords:

GNSS

GLDAS

LSDM

water storage

seasonal

interannual

## ABSTRACT

We systematically investigate the spatiotemporal water storage changes in Taiwan using geodetic (GNSS and GRACE) and hydrological (precipitation, GLDAS and LSDM assimilation models, and in-situ groundwater level) datasets. We use GNSS-observed vertical deformation to estimate water storage changes based on elastic loading theory and weighted least-squares inversion, correcting for contributions from global loads using GRACE. The mean annual water-thickness change inferred from GNSS across Taiwan is  $0.53 \pm 0.17$  m and the largest seasonal change of up to 0.91 m is estimated in southwest Taiwan. Comparison of the geodetic and hydrological data shows that the spatial pattern of annual water storage change estimated from GNSS, GLDAS, and precipitation data are generally consistent, indicating significant seasonal water-load fluctuations in Taiwan. However, the GRACE solution significantly underestimates the amplitude of water mass change in Taiwan due to leakage effect, but temporally correlates well with GNSS estimates. Hydrological assimilation model GLDAS, dominated by shallow soil moisture variations, predicts that the average seasonal variation of water thickness is only about 17% of GNSS estimates. This value is about half of the mean annual LSDM water storage change of 0.18 m including an estimate of both soil moisture and surface water. The discrepancy suggests that the contribution of groundwater is substantial and the total water storage change in the hydrological assimilation model is underestimated in Taiwan. The spatiotemporal distributions derived using independent component analysis (ICA) are generally consistent between the geodetic and hydrological data. However, comparisons of seasonal amplitudes and phases between all data pairs reveal different response times to precipitation, reflecting the complex nature of transient water storage due to variable rainfall patterns, infiltration rate, soil saturation, and runoff. The peak rainfall occurs in June–July, which is one-to-two months before the peak GNSS subsidence. Water storage of the GLDAS model also reaches its maximum in August, suggesting the water storage is controlled by the infiltration rate and capacity and the total water recharge from rainfall is generally larger than discharge in the summer. The highest groundwater levels lag one and two months behind the peak GNSS subsidence in western and eastern Taiwan, respectively, indicating a higher infiltration rate in western Taiwan.

© 2020 Elsevier B.V. All rights reserved.

## 1. Introduction

Water resource is an important issue in Taiwan due to the steep topography and uneven temporal and spatial distribution of rainfall (Fig. 1). The mean annual precipitation in 2005–2016 is about

2580 mm, estimated from the total rainfall over Taiwan divided by area, and only 10%–40% of rainfall contributes to recharge of groundwater (e.g., Lee et al., 2006; Ting et al., 1998). About 70% of rainfall occurs in summer, during monsoon and typhoon season, in contrast to limited rainfall in winter (Fig. 1). Quantifying water storage variability in Taiwan is therefore critical for water resource management. Satellite-based geodetic techniques have proven to be a useful tool not only for measuring crustal deformation and studying plate tectonics, but also for investigating seasonal and

\* Corresponding author.

E-mail address: yaru@earth.sinica.edu.tw (Y.-J. Hsu).

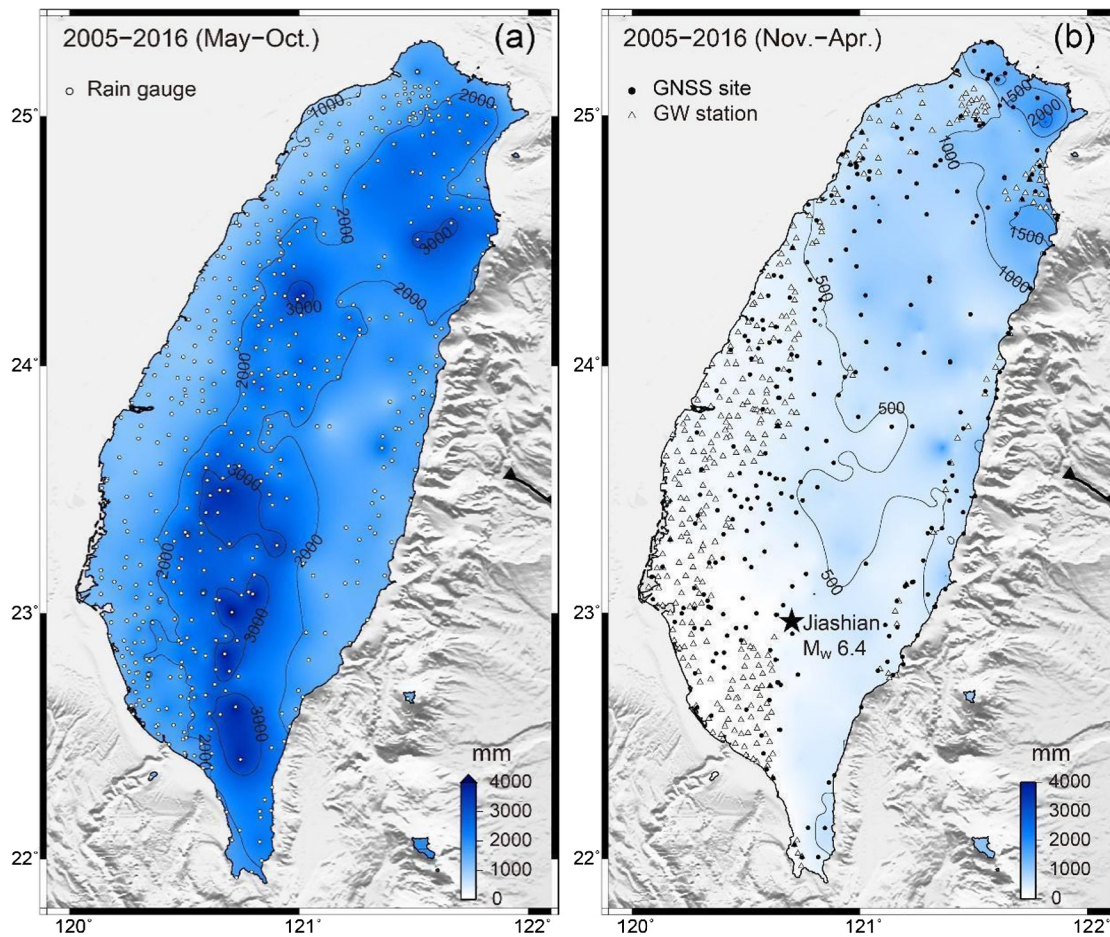


**Fig. 1.** Mean precipitation in the wet (May to October) and dry (November to April) seasons from 2005 to 2016 and distribution of GNSS stations and groundwater level sites. (a) Average total rainfall in the wet season is color coded with a contour interval of 1000 mm. White dots indicate the stations of the Automatic Rainfall and Meteorological Telemetry System. (b) Mean total rainfall in the dry season is color coded with 500 mm contour interval. Circles and triangles show locations of groundwater monitoring well stations and GNSS sites in Taiwan. Black star indicates the epicenter of the 2010  $M_w$  6.4 Jiashian earthquake.

multi-year water storage changes. For example, the Gravity Recovery and Climate Experience (GRACE) mission tracks terrestrial water storage changes by observing the Earth's time-variable gravity variations at  $\sim 350$  km spatial scale (e.g., Tapley et al., 2004; Wahr et al., 2004). Recent progress has been made to infer the water mass changes in the western United States using elastic loading deformation measured from the dense Global Navigation Satellite System (GNSS) network (e.g., Argus et al., 2014, 2017; Borsa et al., 2014; Enzinger et al., 2018; Fu et al., 2015; Johnson et al., 2017). The GNSS results provide water storage change at a refined spatial resolution (several tens of km) than GRACE. In Taiwan, GNSS observations were mostly used for tectonic studies (e.g. Hsu et al., 2009; Yu et al., 1997), and the GNSS-observed vertical deformation shows significant annual and inter-annual variations related to surface water loading effect. But the GNSS measurements in Taiwan have not been systematically analyzed for hydrological applications previously.

The spatial coverage of the continuous GNSS network in Taiwan is dense enough (Fig. 1b) to resolve spatio-temporal water mass changes. GNSS-derived estimates of water mass variations and comparisons with rainfall, groundwater, and hydrological models are very useful for improving the characterization of water storage and transport processes. To validate GNSS inferred seasonal water storage changes and to better understand how water is transferred from the Earth's surface to aquifers, we compare both amplitudes and phases of monthly precipitation, groundwater levels, vertical GNSS displacements, GRACE derived gravity change,

and water storage change estimated from hydrological assimilation models. The integration of data sets covering different temporal and spatial scales provides critical insights into the hydrological factors that influence surface water transport and redistribution. The comparison of different datasets also allows us to evaluate the pros and cons of each approach for estimating water storage variation. As demonstrated later in this paper, the results of our study can only be applied to the regions dominated by elastic loading from water storage changes and do not apply to traditional aquifer systems dominated by alluvial or compressible sediments.

## 2. Data

### 2.1. Precipitation

Rainfall data with 1-hr sampling rate are provided by the Automatic Rainfall and Meteorological Telemetry System (ARMTS) operated by the Central Weather Bureau (CWB), Taiwan. The ARMTS network is composed of more than 750 stations (Chen and Huang, 1999) and data from 562 stations are used to study rainfall characteristics in Taiwan from 2005 to 2016 (Fig. 1a). The annual precipitation of Taiwan ranges from 2000 to 4000 mm, with about 70% occurring from May to September during the monsoon and typhoon season (e.g., Chen and Chen, 2003; Chen et al., 2007). The temporal and spatial distribution of precipitation is extremely uneven in Taiwan. To study seasonality of precipitation, we define the time periods from May to October as the wet season and from

November to April as the dry season. We also define the “hydrological year” as the 12-month period starting from May 1st for any given year to April 30th of the following year to study the annual water cycle. Monthly averaged precipitation data are used for comparisons with other data sets.

## 2.2. Groundwater level

Groundwater is primarily contained in aquifers or porous underground formations and is an important water resource in Taiwan. The installation of a groundwater monitoring network in Taiwan started in 1991 with the primary goal of collecting data for groundwater-resources planning and management. The network is operated by the Water Resources Agency (WRA), Ministry of Economic Affairs (2002) and composed of about 350 stations mostly located in western Taiwan (Hsu, 1998). Each station consists of 1–5 wells to collect the groundwater level data with 1-hr sampling rate from aquifers at different depths. To study groundwater storativity (i.e., the volume of water taken into or released from storage per unit change in water level), we prefer to use deep wells located in the confined aquifer. However, this task is hampered by frequently missing data at deeper wells. Therefore, we only use groundwater levels at the shallowest wells at each station because of the completeness of the observations. While the seasonal amplitudes for wells at different depths vary from 10 m to 20 m, their spatial patterns remain similar (Fig. S1). The time of peak groundwater level (phase) at deep wells is about 15–45 days behind that in the shallow wells (Figs. S1 and S2). We choose 162 stations with continuous records in 2005–2016 (Fig. 1b) and use a least-squares regression with a long-term linear trend and annual terms to extract the amplitude and phase of seasonal groundwater level change. To obtain consistent time series comparable with other data sets, monthly averages are used for comparisons.

## 2.3. GNSS

The Taiwan continuous GNSS array was constructed by the Institute of Earth Sciences (IESAS) since 1990. The network is now composed of more than 400 stations (Fig. 1b) and operated by the Central Weather Bureau (CWB), IESAS, the Central Geological Survey (CGS), and the Ministry of the Interior (MOI). We process local and global continuous GNSS data from 2005 to 2016 with the GAMIT/GLOBK software packages (Herring et al., 2002) and produce a combined daily solution in the ITRF2008 reference frame (Altamimi et al., 2011). We aim to study water storage variation in Taiwan and remove vertical motions associated with the atmospheric, non-tidal ocean, and global hydrological loads from the GNSS time series. The first two corrections use the products from GFZ (<http://rz-vm115.gfz-potsdam.de:8080/repository>) (Dill and Döbslaw, 2013). The loading deformation contributed from all other places on the Earth outside Taiwan is estimated using JPL's global GRACE mascon solution (Watkins et al., 2015) excluding grids over Taiwan. This solution includes degree-1 loading deformation estimated using the spherical harmonic coefficients derived from a combination of GRACE data and geophysical models (Sun et al., 2016). The amplitudes of seasonal motions calculated from these three effects are less than 3 mm (Fig. S3). A least-squares regression is adopted to fit GNSS daily three-dimensional position time series with a linear trend, annual and semi-annual periodic motions, offsets caused by coseismic jumps and instrument changes, and exponential postseismic relaxation following moderate to large earthquakes (Table S1). We only use the vertical data and do not consider the horizontal seasonal motions (Text S1). Estimates of common-mode errors (Dong et al., 2006), the long-term linear trend, coseismic and instrumental offsets, and postseismic relaxation are removed from the raw data (Hsu et al., 2018). We

use the residual GNSS time series to estimate the amplitude and phase of GNSS annual vertical motions.

The majority of continuous GNSS stations (about 95% of 207 stations shown as circles in Figs. 2a, b) in Taiwan reach their lowest height in autumn (late August–September) when surface water storage is at an annual maximum, and attain peak annual uplift in spring (late February to March) during the time of minimum surface water storage. This seasonal cycle of GNSS height series corresponds to the physical loading and unloading effects due to the seasonality of water mass change (Fig. 2). In contrast, 11 GNSS sites located in the alluvial plains show seasonal vertical motions that are in phase with groundwater level change (squares in Figs. 2a and 2b), suggesting a dominant poroelastic mechanism in alluvial plains (e.g., Chaussard et al., 2014). As we are interested in the elastic loading effects, we remove GNSS sites located on alluvial fans and Quaternary basins (Text S2), stations greatly affected by multipath effects based on sky visibility in different years and field photos (Fig. S6), and stations affected by fault creep (Lee et al., 2003) and deep-seated landslides (Hsu et al., 2014). The remaining 176 stations are used to infer the changes of water storage in Taiwan.

## 2.4. Terrestrial water change from hydrological models

We use the Global Land Data Assimilation System (GLDAS: <https://hydro1.gesdisc.eosdis.nasa.gov/data/GLDAS/>) Noah model (GLDAS-Noah2.0) and Land Surface Discharge Model (LSDM) models in this study. The former relies on combinations of multiple land-surface models and meteorological-forcing data sets, integrating the effects of precipitation, solar radiation, air temperature, and other meteorological factors (Rodell et al., 2004). The GLDAS hydrological model provides soil moisture estimates from the surface to a depth of 2 m, snow water equivalent, and a canopy water component, at 0.25° grid spacing and one-month temporal sampling. We combine the sum of these components as the GLDAS water variations. Note that the contributions of canopy and snow water to GLDAS are very small in Taiwan with about 99% of water variations being from soil moisture (Fig. S7). The second model we consider is the LSDM (Dill, 2008; Dill and Döbslaw, 2013), which simulates global water storage and transport in continental regions based on a combination of the Hydrological Discharge Model (HDM) and the Simplified Land Surface (SLS) scheme (Hagemann and Dümenil, 1997; Hagemann and Gates, 2003). The LSDM continental water-storage estimate includes surface water in rivers, lakes, and reservoirs, soil moisture, snow and ice, as well as water in the biosphere. Since the currently available LSDM data do not have a fine resolution to resolve the spatial variation of water storage change in Taiwan, we only use the average result across Taiwan.

## 2.5. GRACE

GRACE measures time-variable global gravity variations and therefore records seasonal water mass changes with a spatial resolution of ~350 km (Tapley et al., 2004). The gravity measurements by GRACE are represented by monthly solutions of spherical harmonic coefficients, which can also be used to estimate surface vertical motions due to surface mass loading (e.g., Davis et al., 2004; Kusche and Schrama, 2005; Fu and Freymueller, 2012). We use the GRACE RL06 monthly gravity solutions provided by the Center for Space Research to estimate monthly water mass variations (Wahr et al., 1998) and model its resulting surface vertical loading displacements (Davis et al., 2004) using the elastic load Love numbers provided by Farrell (1972). We follow the standard GRACE data processing strategy and add the degree-1 coefficients that are estimated using geocenter variations from a combination

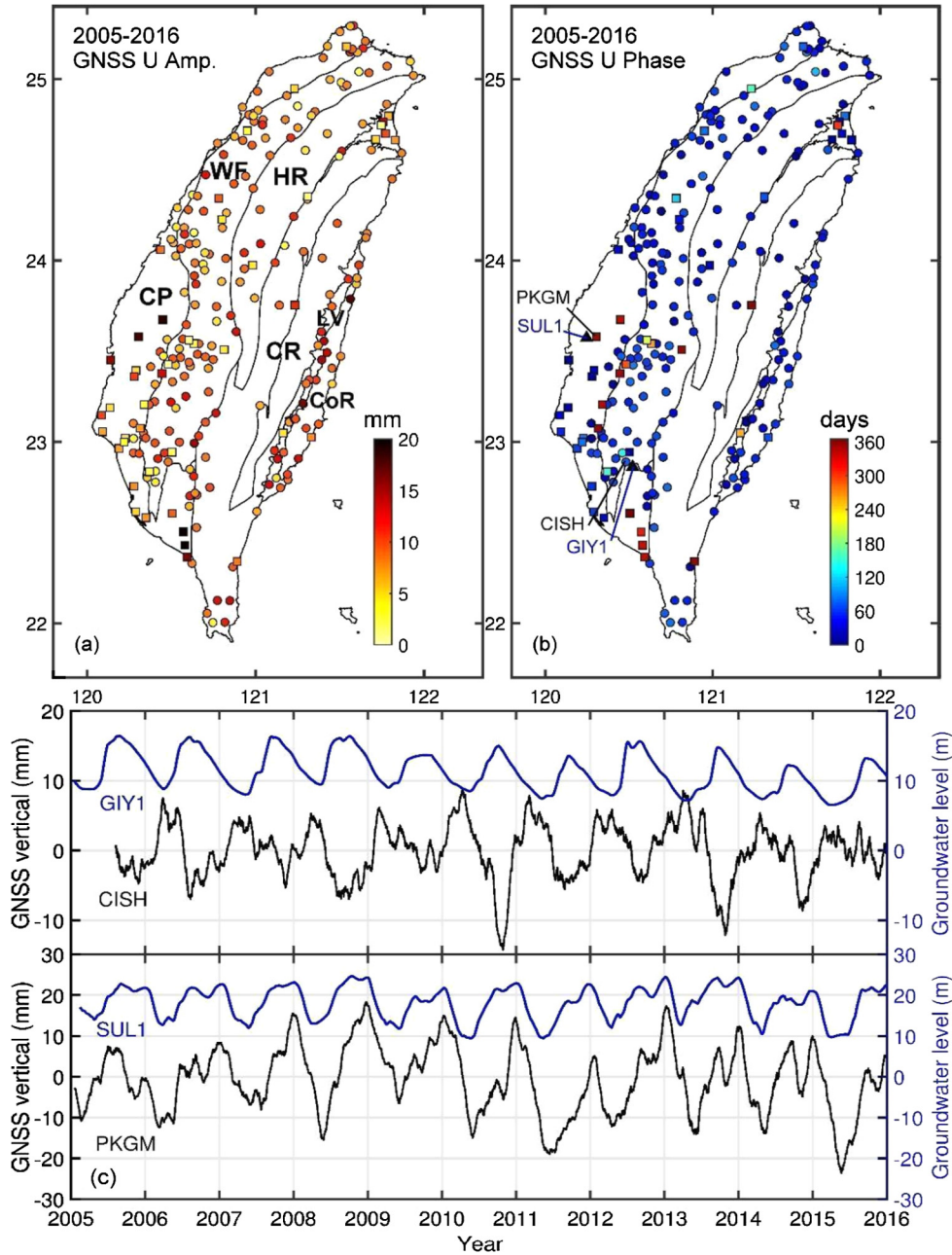


**Fig. 2.** Mean amplitude and phase of GNSS seasonal vertical motion and time series of GNSS and groundwater level data. (a) Amplitude and (b) phase when GNSS reaches peak height. Circles and squares indicate sites dominated by elastic loading and poroelastic response, respectively. Black lines denote the boundaries of six physiographic regions in Taiwan: from west to east, these are the Coastal Plain (CP), the Western Foothills (WF), the Hsueshan Range (HR), the Central Range (CR), the Longitudinal Valley (LV), and the Coastal Range (CoR). (c) Examples of time series of groundwater level (blue) and GNSS (black) at nearby stations (locations marked in (b)) that are out of phase and in phase, reflecting the dominant response to elastic loading and poroelastic deformation, respectively. Groundwater level is measured with respect to the mean sea level.

of GRACE and ocean model output (Sun et al., 2016; Swenson et al., 2008). The major limitation of the GRACE solutions in Taiwan is due to the leakage effect that causes signals to spread spatially and leak into adjacent regions (e.g., Chen et al., 2017).

### 3. Methods

#### 3.1. GNSS inversion model

We next invert for seasonal hydrological loading using 176 GNSS stations and a rectangular grid with  $0.25^\circ$  spacing interval extending from  $120^\circ\text{E}$  to  $122.25^\circ\text{E}$  and  $22^\circ\text{N}$  to  $25.25^\circ\text{N}$ . The elastic vertical loading deformation due to a mass load is estimated by

the Load Love numbers and Green's functions (Wang et al., 2012) based on the Preliminary Reference Earth Model (PREM) (Dziewon-ski and Anderson, 1981). For each grid cell (Text S3), we assume a circular disk load with 1 m water height and 14 km radius that covers the cell, and compute the crustal vertical displacement at each GNSS site corresponding to this load. We employ a weighted least-squares inversion algorithm to minimize the following misfit function:

$$\|W(Gm - d)\|^2 + \beta^{-2}\|\nabla^2 m\|^2 \quad (1)$$

where  $W$  is the weighting matrix equivalent to the inverse of the square root of the data covariance matrix.  $G$  contains the elastic

loading Green's functions relating surface unit load mass change on each grid cell to vertical displacements at each GNSS site.  $m$  is the effective water thickness to be estimated and  $d$  is the amplitude of GNSS annual vertical motion computing from the amplitude of annual periodic motion in least-squares regression. To avoid rapid and unconstrained spatial variations of water mass across adjacent grid cells, we use a Laplacian smoothing operator  $\nabla^2$  and a damping parameter  $\beta$ , which is chosen based on the relative weight between model roughness and data misfit using a trade-off curve (Harris and Segall, 1987). Note that the spatial variation of water storage may not necessarily be distributed smoothly in space. Localized loads (e.g., reservoirs) may dominate the GNSS-observed local loading deformation. We cannot easily invert for the localized load due to the lack of spatial resolution. Fig. S8 shows the inferred effective water thickness without the regularization term in Equation (1) ( $\beta^{-2} \|\nabla^2 m\|^2$ ). Our results indicate that the spatial patterns and the mean value of the effective water thickness estimated from inversions with and without a smoothing constraint are not very different.

### 3.2. Independent component analysis

Here we use the Independent Component Analysis (ICA) method to separate seasonal and interannual signals of the different datasets used in this study. Both ICA and Principal Component Analysis (PCA) are commonly used to analyze large data sets with complex signals in order to reduce the data dimension and recognize primary spatiotemporal features (e.g., Gualandi et al., 2016; Milliner et al., 2018). The PCA aims at decomposing data into orthogonal linear transformations that maximizes the variance of a set of uncorrelated variables whereas the goal of ICA is to find a linear transformation associated with variables that are non-Gaussian and statistically independent. We first analyze our data using PCA and find that it cannot effectively isolate seasonal and multiyear signals. ICA is better in terms of separating GNSS vertical signals with different periods according to our tests (Figs. S9, S10, and S11). We therefore choose the ICA approach which extracts independent components (ICs) of maximum independence instead of considering the minimum correlation adopted by PCA. We use the FastICA algorithm (Hyvärinen and Oja, 2000) to isolate different underlying sources due to its convergence speed and stability. Monthly data are used for ICA and detailed descriptions for data processing and ICA are included in Text S4. The number of ICs used in this study ranges from two to four.

## 4. Results

We first show the spatial distribution of precipitation and GNSS-inferred equivalent water thickness changes and next compare the spatial distributions of seasonal water storage change from GLDAS and groundwater level. To study the features of temporal variations of water storage changes across Taiwan, we stack time series of each dataset (precipitation, groundwater level, GLDAS, GNSS, GRACE) and evaluate the multi-year interannual variations. We next apply the ICA to the groundwater level, GNSS vertical deformation, and GLDAS data in order to investigate spatiotemporal patterns of the different data sets and assess their correlations.

### 4.1. Spatial variation of precipitation and seasonal water storage

The amplitude of mean annual precipitation is  $1.46 \pm 0.69$  m between the dry (November to April) and wet (May to October) seasons. The largest annual change up to 4 m appears in the western foothills of central-southern Taiwan (Fig. 3a). On the other hand, the mean annual GNSS-inferred effective water thickness is

$0.53 \pm 0.17$  m in Taiwan (Fig. 3b). The largest seasonal variation is up to 0.91 m in southwestern Taiwan. Note that the local spatial variations cannot be fully resolved by GNSS due to the insufficient spatial coverage of GNSS sites in the Taiwan mountain belt (HR and CR in Fig. 3b). The amplitude of water mass change in Taiwan estimated from GRACE data is 0.02 m, which is substantially smaller than the estimates from other datasets. This is because of the coarse spatial resolution and significant leakage effect of GRACE solutions for small areas, such as Taiwan. But the GRACE result in Taiwan temporally correlates well with the other datasets (Fig. 4).

We compare GNSS-inferred seasonal water change with the seasonal water variations from the GLDAS-Noah2.0 model (Fig. 3c) and in situ groundwater level measurement (Fig. 3d). Note that the seasonal hydrological loading from GRACE and LSDM are shown in Fig. S12. We did not include them in the comparison due to their low spatial resolution. Seasonal variation of water thickness from the GLDAS-Noah model ranges from 0.05 to 0.15 m, only approximately 17% of the mean water thickness change inferred from GNSS (Fig. 3b). The seasonal fluctuation of groundwater level varies from 1–15 m and its largest seasonal changes are found near the apex of alluvial fans, in and around agricultural areas or fish farms (Fig. 3d). In general, the spatial patterns of annual water mass changes estimated from precipitation, GNSS, and GLDAS-Noah2.0 data are consistent with the largest seasonal water fluctuation in SW Taiwan (Fig. 3). The seasonal amplitude of GLDAS-Noah 2.0, mainly contributed by soil moisture variations, is well below the GNSS-inferred water thickness variation, implying the contributions of groundwater, reservoir water, surface water, and soil moisture at depths larger than 2 m are substantial in Taiwan. Previous studies also found similar results in the Western United States where GLDAS also underestimates total water storage changes (Argus et al., 2014; Fu et al., 2015). When we consider the mean annual LSDM water storage change including soil moisture and surface water, the mean seasonal amplitude is 0.18 m, reaching about 34% of the GNSS-inferred water thickness change. The spatial variability of seasonal groundwater level change is very different from the other measurements and is likely associated with the sparse distribution of groundwater stations, the local human groundwater use and/or heterogeneity in storativity (Chen et al., 2018; Kuhlman et al., 2008).

Rainfall is the primary source of water in Taiwan. Due to the steep topography and large rainfall intensity in Taiwan, a large portion of precipitation contributes to rapid runoff rather than infiltration and subsurface storage. By comparing different water storage change estimates (Fig. 3), we can approximately quantify the partitioning between water infiltration, temporary surface water storage, and runoff. The inferred water thickness from GNSS is presumably a proxy for the total water storage assuming that contributions from other sources (ocean loading, atmosphere, loading deformation due to mass changes outside Taiwan, poroelastic, draconitic signal etc.) have been successfully mitigated. The mean amplitude of GLDAS-Noah2.0 is 0.09 m (Fig. 3c) which mainly consists of soil moisture changes. The annual change of LSDM in Taiwan is 0.18 m which is primarily from soil moisture and surface water. Therefore, shallow soil moisture and surface water both contribute about 17% of total water storage. A considerable fraction of 66% for total water variation may include contributions from deep (>2 m) groundwater or other sources. They may also reflect substantial underestimates of annual water storage changes in the hydrological assimilation models. Estimates of the water storage from 18 major surface reservoirs in Taiwan contribute no more than 8% of total water storage change (Text S5). If we consider soil moisture contributes about 50% of the LSDM-model storage, then surface water (in rivers, lakes, and reservoirs) contributes another half. The contribution from the latter is likely to be underestimated. More-

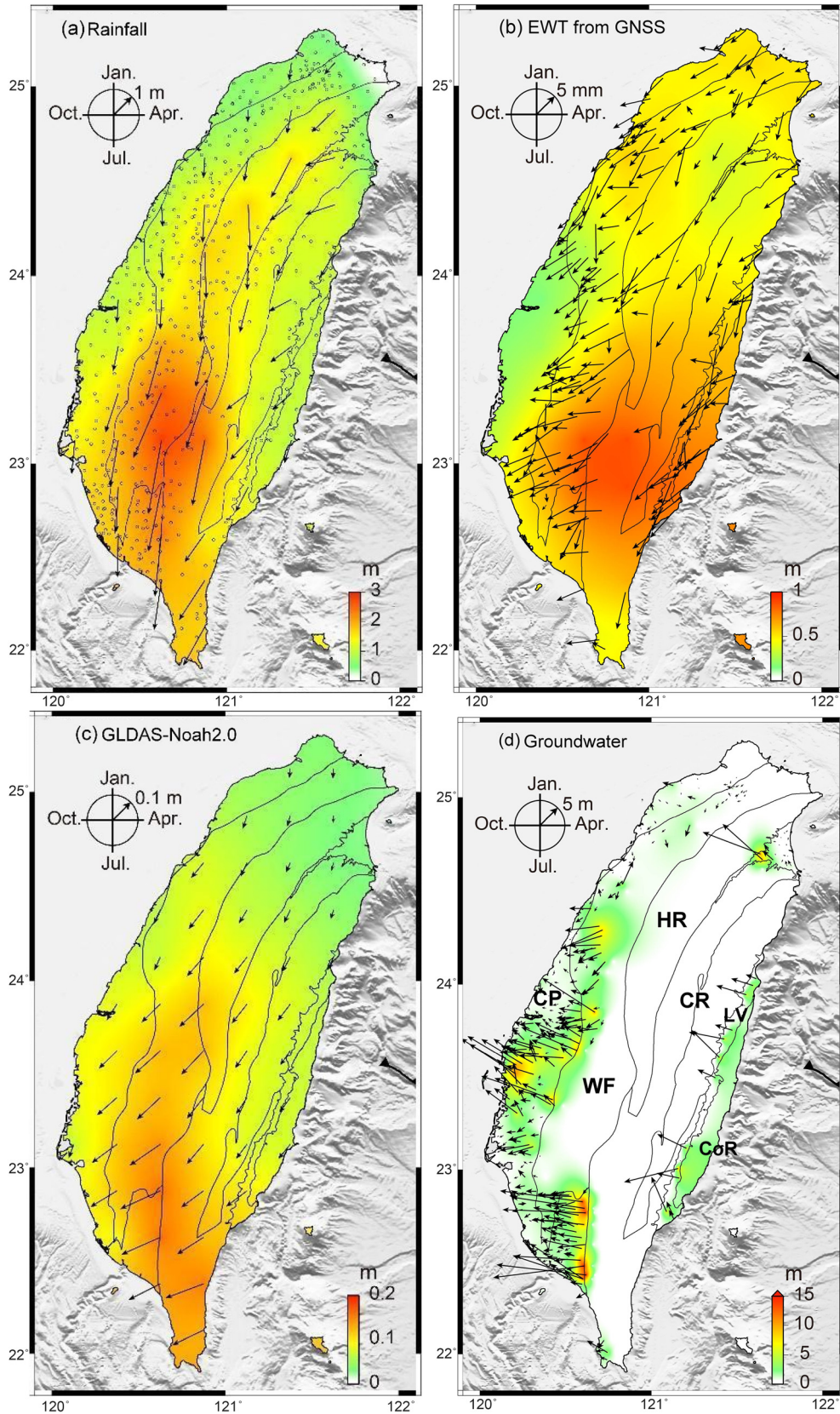


**Fig. 3.** Amplitude and phase of the mean seasonal water change from 2005 to 2016. Black lines denote the boundaries of six physiographic regions in Taiwan (same as in Fig. 2a). (a) The mean annual amplitude and phase in precipitation between the wet and dry seasons, (b) in effective water thickness inferred from GNSS, (c) in soil moisture from GLDAS-Noah2.0, and (d) in groundwater level measured at monitoring wells.

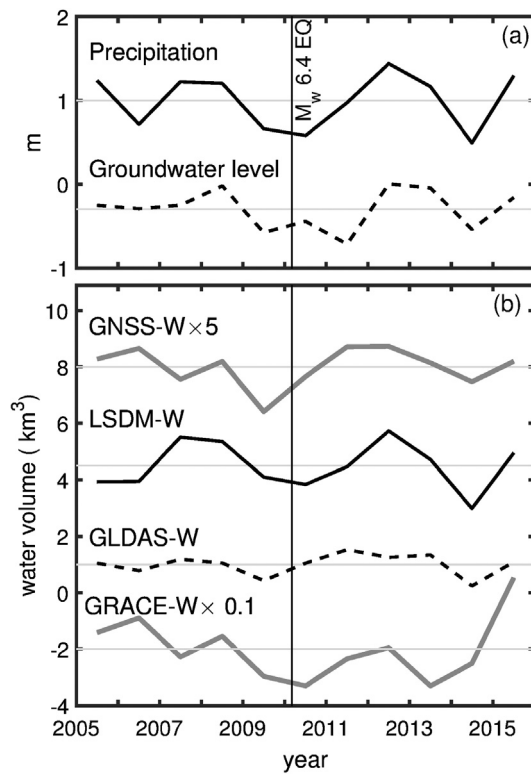


**Fig. 4.** Interannual variations in stacking time series of precipitation, groundwater levels, GNSS-W (Water change), LSDM-W, GLDAS-W, and GRACE-W data averaged across Taiwan from 2005 to 2016. Lines shows detrended time series estimated using a consecutive one-year sampling window within a hydrological year (May 1st–April 30th) from various data sets. The curves are offset for clarity. Vertical line indicates the time of the 2010  $M_w$  6.4 Jiashian earthquake.

over, we estimate the seasonal storage efficiency (Fig. S13) from the ratio of GNSS-inferred water thickness changes (Fig. 3b) to the annual amplitude of precipitation (Fig. 3a). The ratio varies from 20% to 60% in areas with good spatial coverage of GNSS sites. We find the water retention in eastern Taiwan is slightly larger than that in western Taiwan, which is likely associated with the less urbanized landscape and the less water use in agriculture in eastern Taiwan. Despite the steep topography in Taiwan, the spatial pattern of annual precipitation between the dry and wet seasons is generally consistent with water storage from GLDAS-Noah 2.0 and effective water thickness derived from GNSS vertical displacements, suggesting the amount of infiltrated water scales with rainfall and is less influenced by topography. The high infiltration capacity in steep mountain areas may be due to high forest coverage and highly permeable soils (Cheng et al., 2002).

#### 4.2. Temporal variation of water storage

Investigating interannual and seasonal changes of water storage can provide critical insights into the water cycle process. To study the features of temporal variations of water storage changes across Taiwan, we first stack time series of each dataset, remove the long-term trend, and then evaluate the multi-year interannual variations. In section 4.3 below, we will apply the ICA to further characterize the spatiotemporal patterns of different water storage datasets. Fig. 4 shows detrended and stacked time series of precipitation, groundwater levels, LSDM-W (LSDM-derived Water change), GLDAS-W, GNSS-W, and GRACE-W. The water change is calculated from the product of the area of Taiwan ( $36,193 \text{ km}^2$ ) and the effective water thickness (EWT). The time series are estimated within a hydrological year (May 1st–April 30th, defined in Section 2.1), which is chosen to minimize seasonal variations. Af-

ter removing the linear trends, heavy precipitations in 2007–2008 and 2012–2013, which generally correspond to high groundwater levels, LSDM-W, and GLDAS-W in the same periods (Fig. 4). The temporal variation in GNSS-W and GRACE-W due to the wet periods is less prominent compared to other data sets but relatively higher peaks can be found in 2008 and 2012. The troughs due to the dry periods in 2009–2010 and 2014 are evident in all data sets, except for the dry year of 2014, which shows an increase in GRACE-W. The interannual water change over periods of dry and heavy precipitation can be up to  $9 \text{ km}^3$  in GNSS-W and  $2.7 \text{ km}^3$  in LSDM-W. The GNSS-W exhibits an increasing trend in 2010, which is not likely associated with hydrological signals (Text S6). The correlation coefficients between different data sets are about 0.3–0.8 (Table S2) and can be improved to 0.5–0.8 when we ignore GNSS-W and GRACE-W data. Note that the interannual time series do not show time lags between the different data sets.

#### 4.3. Spatial and temporal patterns estimated from ICA

To better resolve the spatiotemporal water storage variations, we decompose the groundwater level, GNSS, and GLDAS-Noah2.0 time series using the ICA technique. Fig. 5 shows the four ICs derived from groundwater level data. The variance reduction for the four ICs is 65%. Fig. 5a shows the time series of groundwater level contributed by each IC, and the percentage of contribution to the variance is shown in the top right corner of each panel. The phases of the annual peaks for IC 1 and IC 2 are around DOY (day-of-year) 305 and DOY 215, respectively. This feature is likely related to the double rainy seasons in Taiwan (e.g., Chen, 1992; Wang et al., 1994), which involve typhoons in August–September and the Meiyu period in mid-May to Mid-June (Fig. S14). When a component has an annual peak in a similar period of the year, we consider this component to be seasonal. The IC1 and IC2 show mostly seasonal changes and their combination explains 80% of total variance in the filtered time series and best represents the seasonal variation of groundwater level. We estimate the average phase of seasonal water level changes by fitting annual sine and cosine functions to the combined IC time series, and find the annual peak occurs at DOY 270 (early October), consistent with the median peak on DOY 265 estimated from a least-squares regression using time series of groundwater level. The spatial pattern of seasonal changes shows large variations at stations located in and around the apex of the alluvial plain, similar to the results shown in Fig. 3d. The IC3 shows a long-term decreasing trend in most areas of the west coastal plain. The IC4 is likely related to an interannual variation of precipitation (Fig. 5a). Heavy precipitation in 2012–2013 causes the groundwater level rise in NW Taiwan and the Choushuichi alluvial plain whereas a slight decline of groundwater level at the same period is found in the Pingtung plain due to reduced precipitation in that area.

For the GNSS vertical displacement series, we consider four ICs which provide a combined variance reduction of 57% (Fig. 6a). The ICs 1–2 show mostly seasonal motions and the phases of annual peak for IC1 and IC2 are around DOY 37 and DOY 123, respectively. The GNSS ICs 1–2 are likely corresponding to IC2 (DOY 215) and IC1 (DOY 305) in groundwater level due to the double rainy seasons in Taiwan (Fig. S14). The sum of ICs 1–2 best represents the seasonal variation and explains 80% of the total variance in the filtered time series. The average peak of GNSS seasonal vertical motion due to water loss appears in DOY 75 (March), consistent with the peak DOY 55 estimated from a least-squares regression. The ICs 3–4 show mostly interannual variations and IC 3 has a significant response to the dry period of 2014–2015 (Fig. 4). Spatial patterns of ICs 3–4 are heterogeneous with both positive and negative responses. Most stations in SW Taiwan show significant uplift during the water loss in 2014–2015.

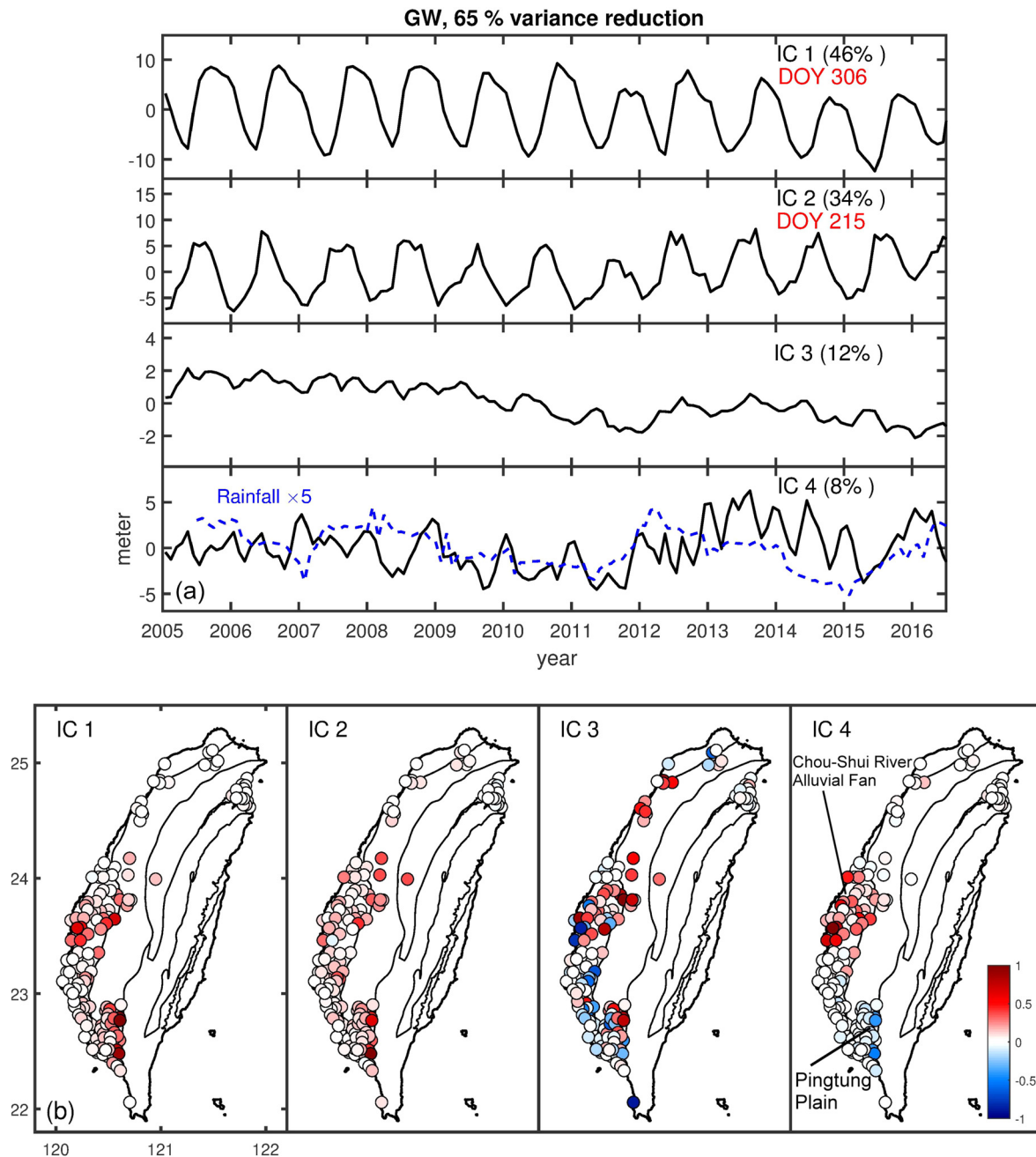


**Fig. 5.** Independent components (ICs) of spatial and temporal variations for groundwater level data from 2005 to 2016. The top panel (a) shows the temporal evolution of each IC in meter. The variance reduction from the 4 ICs is 65% and the percent contribution of each IC to the filtered time series is shown by black text labels in each panel. Red text indicates the time of annual peak in DOY (day-of-year). Blue dash line denotes moving-average rainfall with a 12-month window and time shift of one month. Four panels in (b) show the spatial response of ICs 1-4, respectively. The product of temporal and spatial weights provides the time series of groundwater level contributed by each IC.

The ICA decomposition of water storage estimates from GLDAS-Noah 2.0 is shown in Fig. 7. Two ICs can explain 83% of data variance. The seasonal fluctuation is best explained by the IC 1 with the peak of water storage in DOY 230, consistent with the peak of DOY 220 in regression results. The spatial pattern indicates a large variation of water storage in SW Taiwan, similar to the spatial distribution of annual water change from GNSS-inferred water thickness and precipitation observations (Fig. 3). The IC2 shows a sharp decrease of GLDAS-Noah 2.0 in 2016, opposed to the increase of water shown in the other data sets (Fig. 4). The reason is unknown but might be caused by the underestimation of some water components in the GLDAS model (e.g., Fu et al., 2015).

## 5. Discussion

### 5.1. Model resolution

In order to evaluate the spatial resolution of GNSS inferred effective water thickness, we perform checkerboard resolution tests using the locations of GNSS sites and data covariance matrix adopted for the inversion in Section 3.1. The input checkerboard pattern and output model are shown in Fig. 8. Results of these tests demonstrate that the inversion is able to resolve water storage change in northern and western Taiwan, recovering about 60%-70% of the input water thickness. In the Longitudinal Valley, the spatial resolution is lower than that in western Taiwan since most

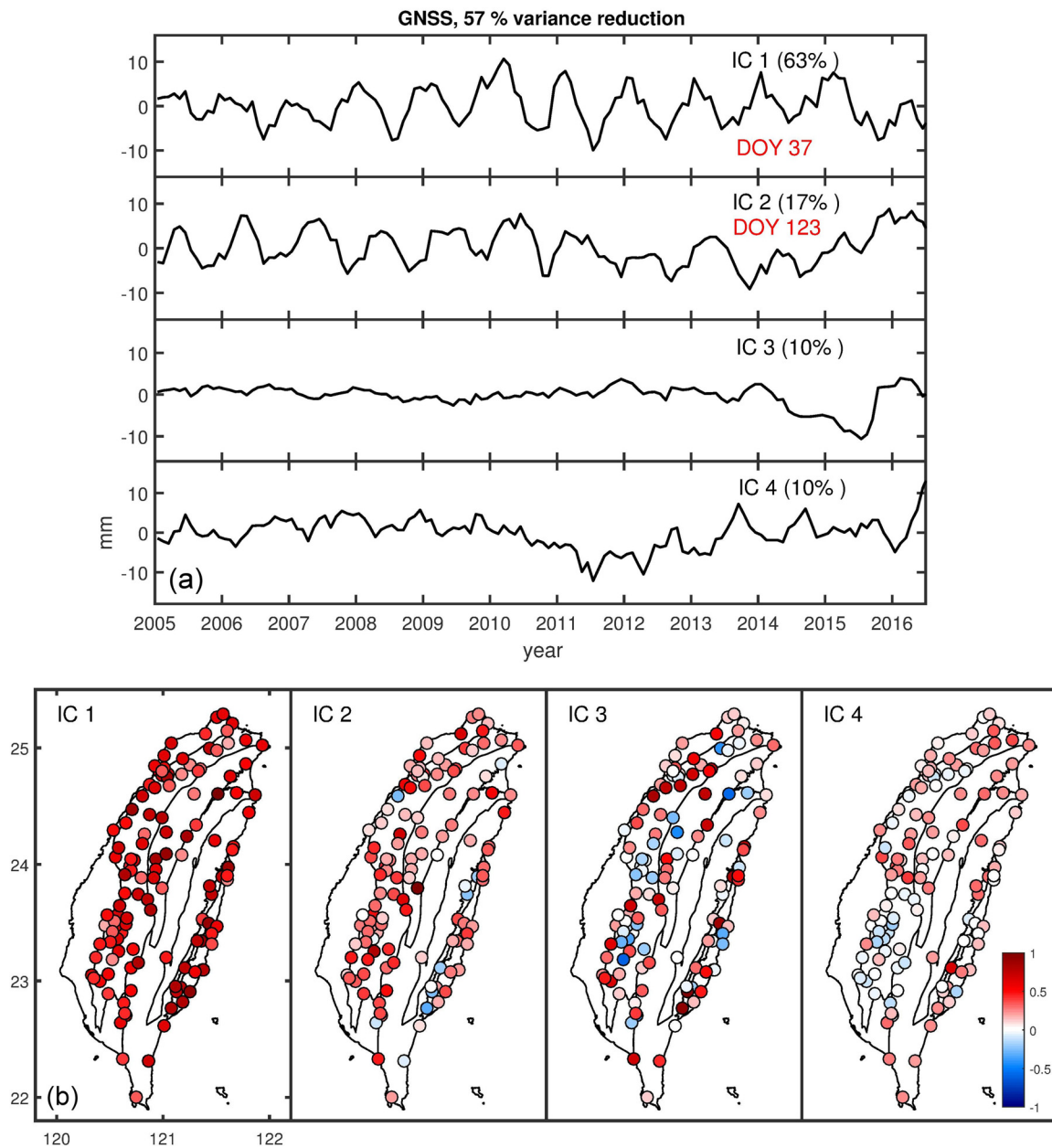


**Fig. 6.** Independent components (ICs) of spatial and temporal variations for GNSS vertical position time series from 2005 to 2016. Stations whose time series are dominated by poroelastic response (squares in Figs. 2a and 2b) are excluded. The top panel (a) shows the temporal response of each IC. The variance reduction from the 4 ICs is 57% and the percent contribution of each IC to the filtered time series is shown by black text labels in each panel. Red text indicates the time of annual peak in DOY (day-of-year). Four panels in (b) show the spatial response of ICs 1–4, respectively. The product of temporal and spatial weights provides the time series of GNSS vertical motion contributed by each IC.

continuous GNSS stations are distributed in a narrow strip. Spatial resolution in the Central Range of Taiwan is generally poor with amplitudes off by  $\sim 50\%$ , but the overall pattern is adequately resolved. For the checkers with less than 3 GNSS stations, the resolution is generally unsatisfactory.

### 5.2. Time-variable seasonal amplitudes changes

We obtain similar spatial patterns for annual precipitation change, the GNSS-inferred water thickness, and soil moisture from GLDAS (Fig. 3). To investigate temporal variations of seasonal water change, we compare changes of seasonal amplitudes extracted from different datasets (Fig. 9a). The annual fluctuation of GNSS-EWT is derived from GNSS vertical position time series (ICs 1–2). The GLDAS-Noah2.0 (IC 1) and groundwater level (ICs 1–2) are es-

timated from the summation of the products for the temporal and spatial eigenvectors. For seasonal variability of rainfall, LSDM-EWT, and GRACE-EWT, we use a consecutive one-month sampling window (Fig. 9a). Table 1 lists cross-correlation coefficient ( $cc$ ) and time lag between seasonal variations extracted from various data sets. Estimates of  $cc$  between different data pairs range from 0.3 to 0.8 with time lags of 1–2 months. The linear relationship between seasonal precipitation and other data sets is weak with  $cc$  of 0.3–0.7. In contrast, other data pairs show stronger linear correlations with  $cc$  of 0.5–0.8. In general, precipitation first reaches its seasonal maximum, and then GLDAS, GNSS-EWT, LSDM-EWT, groundwater level, and GRACE-EWT subsequently attain their annual peak within 0–2 months (Table 1, Figs. 9a and S16). During the 2005–2016 study time period, the minimum water storage occurred in early 2011 and 2015 (shaded red bands in Fig. 9a).

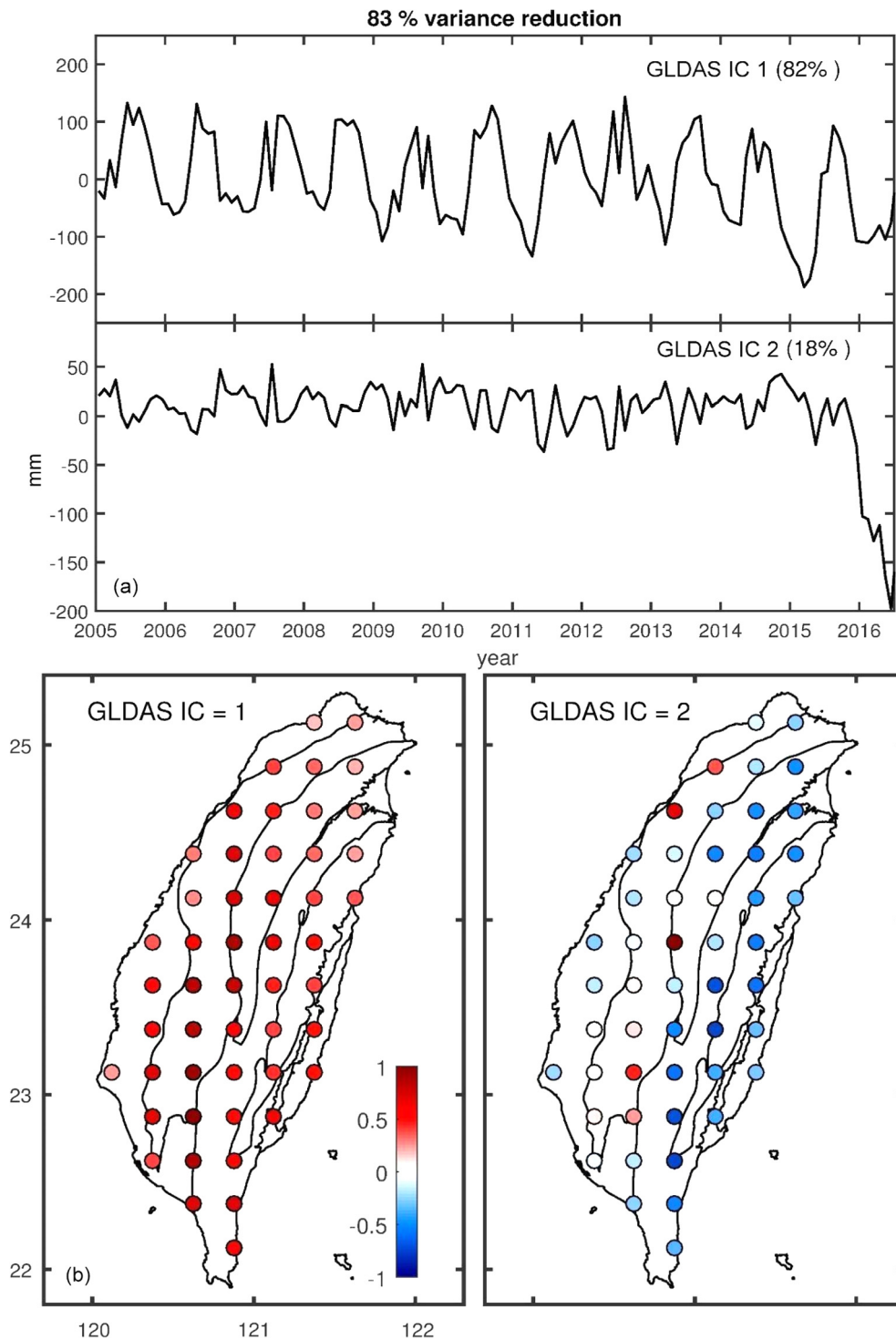


**Fig. 7.** Independent components (ICs) of spatial and temporal variations for total water storage from GLDAS-Noah 2.0 from 2005 to 2016. The top panel (a) shows the temporal response of each IC. The variance reduction from the 2 ICs is 83% and the percent contribution of each IC to the filtered time series is shown by text labels in each panel. Two panels in (b) show the spatial response of ICs 1-2, respectively. A sharp decrease of IC 2 near 2016 may indicate some problems in GLDAS-Noah2.0 in that period.

The lowest GNSS-EWT near 2010 results from GNSS subsidence at many stations distributed across all of Taiwan, whose cause remains unclear (Text S6). Fig. 9a shows that the temporal variations of seasonal amplitude changes for precipitation observations, groundwater level, and LSDM-EWT, GLDAS are similar.

We also estimate the interannual trends of GNSS-EWT from GNSS vertical time series (ICs 3+4), GLDAS (ICs 1+2), and groundwater level (ICs 3+4) series, respectively, within a hydrological year (Fig. 9b). To compare with the interannual variations of rain-

fall, LSDM-EWT, and GRACE-EWT, we remove the long-term linear trends in ICA time series of GNSS-EWT, GLDAS, and groundwater level. If we ignore the unclear GNSS motion around 2010, the interannual trends of most data sets show a generally consistent temporal pattern. The water gain in 2007-2008 and 2012 to 2013 as well as the water loss in 2009-2010 and 2014 to early-2015 are evident in the majority of data sets.

Compared with rainfall, LSDM-EWT, GLDAS, and GRACE-EWT datasets, groundwater and GNSS-EWT observations show a time

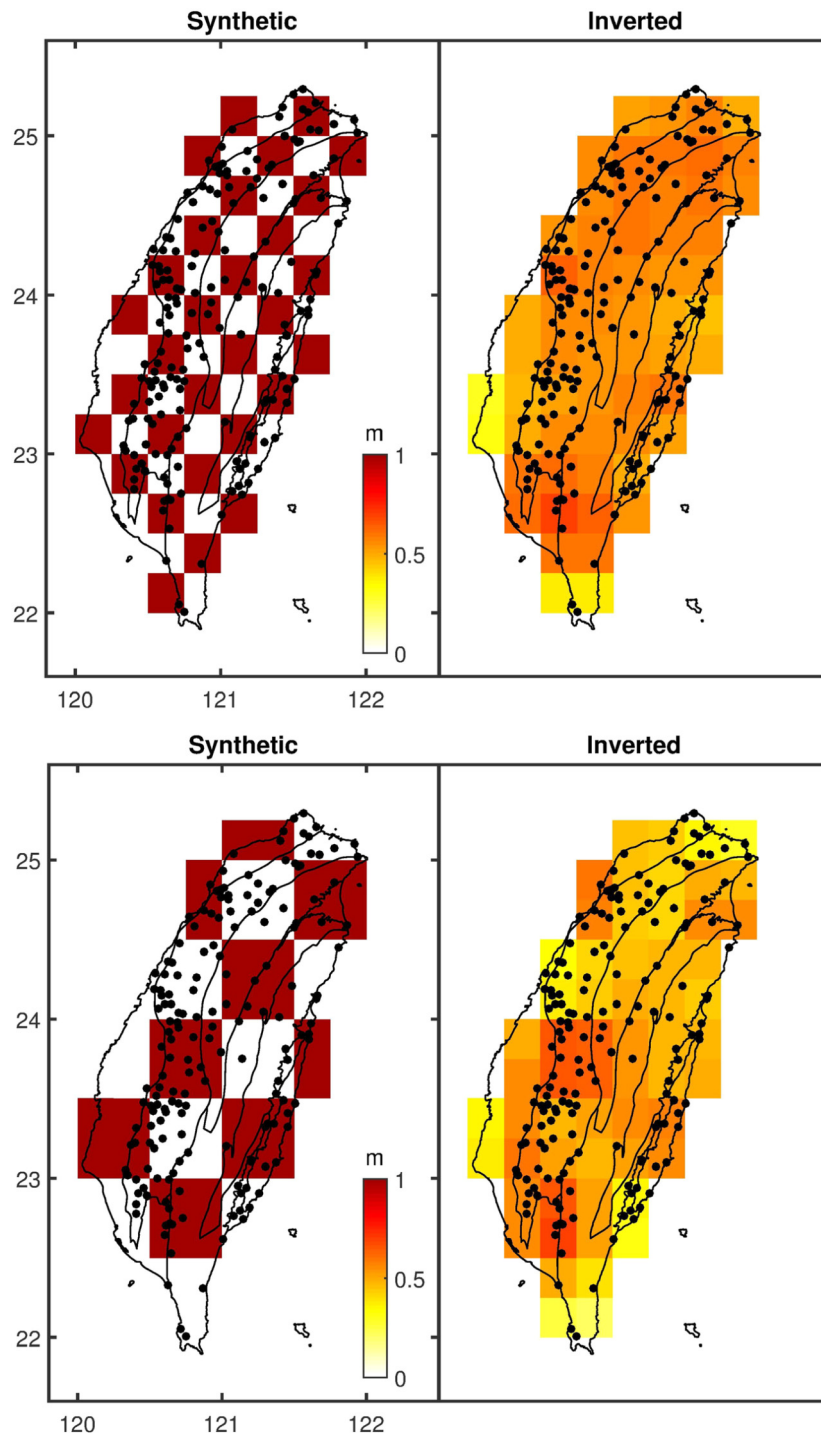


**Fig. 8.** Checkerboard tests for inversion of elastic model deformation from the synthetic load pattern. Two distributions of input load with  $0.25^\circ$  and  $0.5^\circ$  spatial patterns are performed. The inversion with  $0.5^\circ$  spacing can recover 60%–70% of input water thickness in northern and western Taiwan with dense GNSS network station spacing.

lag of about one year during the wet periods from 2011 to 2013 (Fig. 9b). For the dry year of 2014, the minimum of GNSS-EWT and groundwater level both occur in 2014–2015 whereas the minimum of GRACE-EWT appears at the end of 2013 (Fig. 9b). Since GNSS and GRACE are presumably measures of total water storage, the time lag between them is not expected. Note that the seasonal peak of GRACE-EWT also shows a one-month lag behind the annual peak of GNSS-EWT (Table 1 and Fig. S15). One possible explanation may be the different spatial sensitivities of GNSS and GRACE to water changes. A single GNSS loading displacement is mainly affected by local loads within 100–200 km (e.g., Bevis et al.,

2005) whereas GRACE has a much coarser spatial resolution, as evident by the mean seasonal amplitude of 0.02 m for GRACE-EWT, about 4% of the average annual amplitude of GNSS-EWT (Fig. S15).

Since dry periods in Taiwan often occur in winter and spring due to the lack of precipitation in the previous wet summer season, we estimate the annual change of seasonal amplitude as the difference between the maximum value from July to December of the given year and the lowest value from January and April in the following year. Therefore, we can obtain estimates of the seasonal amplitude within a hydrological year. Even though precipitation is commonly used to quantify water resources, precipitation changes

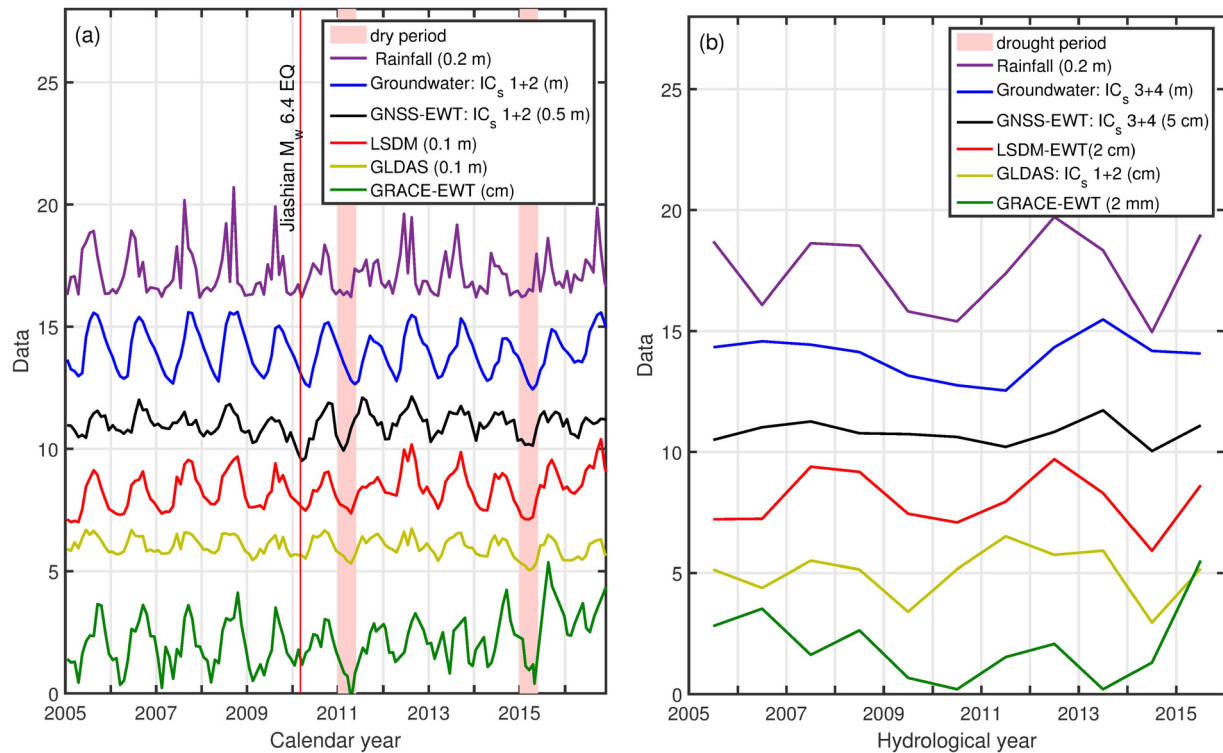


**Fig. 9.** Temporal variations of average seasonal and interannual water storage for different geodetic and hydrological datasets from 2005 to 2015 using ICA. See legend for scale and data units. (a) Time series of seasonal changes derived from ICA. Red shaded band denotes the dry period. Comparisons of seasonal amplitudes and phases between all data pairs reveal different response times to precipitation, reflecting the complex nature of transient water storage due to variable rainfall patterns, infiltration rate, soil saturation, and runoff. (b) Interannual changes derived from ICA in each hydrological year.

**Table 1**

Estimates of cross-correlation coefficient ( $cc$ ) and time lag between seasonal motions with one-month sampling rate extracted from various data sets with the ICA (Fig. 9a). The first number is  $cc$  and the second number is time lag in months. The phase shift is the column parameter relative to the row parameter. Negative number means seasonal peak of the column parameter is ahead of the row parameter and vice versa.

	Precipitation	LSDM-EWT	GRACE-EWT	GLDAS	Groundwater level (GW)
GNSS-EWT	0.31/-1	0.60/0	0.52/1	0.60/0	0.65/1
Groundwater level (GW)	0.42/-2	0.80/-1	0.68/0	0.77/-1	
GLDAS	0.43/0	0.66/0	0.52/1		
GRACE-EWT	0.44/-2	0.71/0			
LSDM-EWT	0.67/-1				

between the dry and wet seasons do not show a good correlation with the remaining data sets (Table 1). The poor correlation between net annual rainfall and the various measures of water storage is likely owing to the larger precipitation rate compared to the infiltration rate and the large amount of runoff flowing quickly into the ocean before being recorded.

### 5.3. Spatial pattern of time-variable seasonal amplitudes

Additionally, we compare the spatial pattern of seasonal oscillation and its variability after removing the average from the hydrological years (May 1st–April 30th) 2005 to 2015. The spatial patterns of time-variable seasonal amplitudes in precipitation, GLDAS and GNSS-EWT are similar to the average result shown in Fig. 3. The annual water storage changes illustrated in precipitation and GLDAS exhibit larger annual fluctuations in western Taiwan compared to the east, with the largest annual variation concentrated in central to SW Taiwan (Figs. S16 and S17). The contrast of annual variability between western and eastern sides of Taiwan is less prominent in GNSS-EWT (Fig. S18). Taiwan experienced two

relatively dry periods in 2005–2016, including the first half of 2011 and the extreme dry period in early-mid 2015, corresponding to the hydrological years of 2010 and 2014. We find relatively low precipitation in 2010–2011 and 2014–2015 (Fig. S16) in contrast to high annual water changes in GLDAS in the hydrological years of 2010 and 2014 (Fig. S17), which are different from our expectation that annual water storage change scales with annual precipitation as found in the western U.S. (Fu et al., 2015). We postulate that soil moisture at depths of 0–2 m provided by GLDAS model only represents water storage in the shallowest reservoir which is already saturated from moderate rain and/or the precipitation rate is larger than the maximum rate of infiltration and the excess water becomes surface runoff. Therefore, the large precipitation in 2012 does not result in an increase of peak annual amplitude compared to other years (Fig. 9a).

Variability of GNSS-EWT also indicates a large water storage change during 2010 and a modest variation in 2014 (Fig. S18), opposite to the expectation from our hypothesis that water storage change is proportional to the amount of precipitation. We consider several possibilities to explain this disagreement. The larger-than-normal elastic ground uplift may occur due to the significant water loss in dry years, so the computed GNSS-EWT is substantially increased. On the other hand, during especially wet years, enhanced runoff and limited storage capacity in soil moisture, surface- and groundwater systems may moderate the seasonal amplitude as well. It is also important to keep in mind that the GNSS time series could be biased by other sources of annual deformation. In addition to elastic loading due to surface water storage change, GNSS measurements may be influenced by local poroelastic effects from massive pumping of groundwater during the dry years. The poroelastic effect is presumably controlled by the thickness of unconsolidated sediments. Previous studies suggest that unconfined aquifers and deep water in bedrock do not produce significant poroelastic deformation (Argus et al., 2017). Although we remove

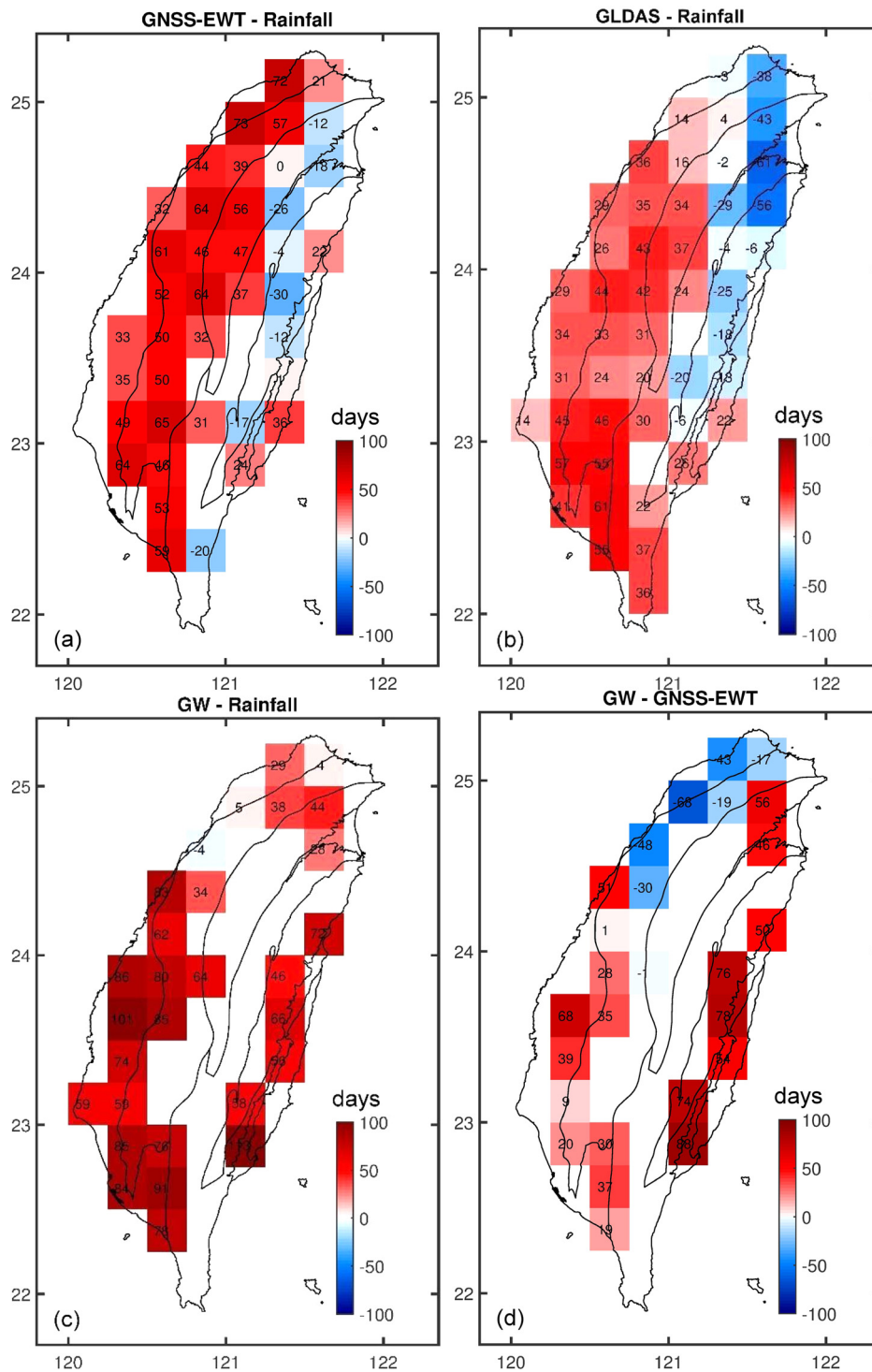


**Fig. 10.** Spatial distribution of phase difference of the annual peaks among different data pairs. GW represents groundwater level. Note that the peaks of (a) GNSS-EWT and (b) GLDAS precede the peaks in precipitation (September) in NE Taiwan. The primary water resource in NE Taiwan comes from mountains in northern Taiwan where rain gauges show the peak rainfall in July-August.

GNSS sites located on alluvial fans and Quaternary basins to minimize the influence of poroelastic effects, some stations close to these areas may still have been affected. Other potential sources of seasonal signals are discussed in Text S7.

#### 5.4. Differences in phase between precipitation and storage parameters

Time lags between precipitation, groundwater level, and surface deformation presumably provide important constraints for the

complex dynamic processes involved in water storage and transport. Fig. 3 shows the average phase of peak seasonal motion from different observations. Since the time series of precipitation often shows a saw tooth pattern, we use a consecutive one-month sampling window to estimate the phase of the seasonal peak. Heavy precipitation occurs in June-July in western Taiwan and is about one month ahead of the largest rainfall in eastern Taiwan. Based on climatology data, the precipitation peak in June-July in western Taiwan is mainly due to the southwesterly monsoon rainfall

in the Meiyu season (Chen, 1992), and the rainfall peak in eastern Taiwan in August is attributed to typhoons in late summer (Wang et al., 1994). Both the peaks of GLDAS model estimates and GNSS-EWT in western Taiwan occur in August–September, and do not show a significant difference between western and eastern Taiwan (Figs. 3b, c). In western Taiwan, the peaks of GLDAS and GNSS-EWT lag one to two months behind the largest rainfall (Figs. 10a and 10b) and the peak of groundwater level lags two to three months behind the summer heavy rain (Fig. 10c). The time lag implies a large amount of excess rainfall quickly flows into the ocean in July, as longer-term subsurface water storage grows. This is also confirmed by GNSS-derived seasonal water storage changes being a fraction of the annual precipitation input (Fig. S13). In addition, the larger watershed and 18 major reservoirs in western Taiwan imply a higher storage capacity, taking longer time to fill up. Note that the peaks of GLDAS and GNSS-EWT precede the largest rainfall in NE Taiwan because the primary water source comes from northern mountains where peak rainfall occurs in July–August.

The heavy rainfall in June and July fails to maximize the GLDAS-model storage in shallow soil layers and vegetation, owing to an upper bound on the recharge rate controlled by the infiltration capacity, which is much less than the heavy rainfall intensity. The hypothesis of an upper limit on the recharge rate is also supported by Fig. 9a and the poor cross-correlation between the amplitude of rainfall and GLDAS (Table 1). That is, the increase of rainfall during the wet years, such as 2012, does not lead to a significant rise in water storage captured by the GLDAS model. Since the water storage has not reached its capacity after the first wet period (June and July), the high rainfall brought by summer typhoons during August and September results in additional water gain in Taiwan. The continuous increase of water storage suggests that the recharge from rainfall in this period (August and September) is still larger than the total water discharge to the ocean via rivers and to the atmosphere through evapotranspiration. The water storage finally reaches its maximum by the end of September.

The data shows a one-month lag between the peaks of precipitation in western and eastern Taiwan, but the annual peaks of GNSS-EWT and GLDAS are both close to August–September (Fig. 3). In Taiwan, the total water content on both sides reaches a maximum after the typhoon-related heavy rainfall throughout the whole summer. The highest groundwater level is about one month and two month behind the peak of GNSS-EWT on the western and eastern sides of Taiwan, respectively (Fig. 10d), suggesting a faster downward water movement or percolation in the vadose zone in western Taiwan compared to that in eastern Taiwan. The phase shift reflects the time for the infiltrated water to move from the shallow vadose zone to the saturated zone below the groundwater table. The temporal patterns of GNSS-EWT and groundwater level data provide a novel way to estimate the quantity and residence time of water in the vadose zone and is worthy of further investigation in the future.

## 6. Conclusions

Our study indicates that geodetic data, including GNSS-derived deformation and GRACE gravity measurements, hydrological assimilation models and in-situ groundwater observations consistently show significant and complicated water storage variations in Taiwan, both spatially and temporally. GNSS vertical loading deformation from the dense network in Taiwan is demonstrated to be capable of quantifying water storage change, although the local spatial variation in the Central Range is not well resolved due to insufficient GNSS station coverage. Mean annual water storage change across Taiwan estimated from GNSS is 0.53 m with a maximum of 0.91 m in SW Taiwan. While GRACE gravity time series appear to capture the temporal pattern of total surface mass load

changes well, the small size of Taiwan causes leakage problems that lead to a severe underestimate of the amplitude of the water storage cycles. The spatiotemporal patterns of seasonal water storage and interannual trends extracted from precipitation, GNSS, and GLDAS Noah 2.0 are very similar. The phases of peak seasonal water storage derived from various data sets reflect the spatially variable infiltration capacity and landscape across Taiwan.

Efficient management of water resources in Taiwan is of paramount importance and the monitoring of the water resource redistribution should be accurate and in real time. Incorporating GNSS loading deformation, LSDM, GLDAS, and GRACE gravity change into an integrated water monitoring network provides independent information on net storage changes. The development of optimal strategies combining hydrological and geodetic measurements and models still needs further investigation.

## CRedit authorship contribution statement

**Y.-J. Hsu:** Conceptualization, Formal analysis, Investigation, Writing - original draft, Project administration, Funding acquisition. **Y. Fu:** Conceptualization, Formal analysis, Writing - reviewing and editing. **R. Bürgmann:** Conceptualization, Writing - reviewing and editing. **S.-Y. Hsu:** Investigation, Editing. **C.-C. Lin:** Investigation. **C.-H. Tang:** Investigation. **Y.-M. Wu:** Resources.

## Declaration of competing interest

The authors declare that they have no known competing financial interests or personal relationships that could have appeared to influence the work reported in this paper.

## Acknowledgements

We are grateful to many colleagues at the Institute of Earth Sciences, Academia Sinica, who have participated in collecting continuous GNSS data. The generous provision of continuous GNSS data from the Central Weather Bureau, the Central Geological Survey, and the Ministry of the Interior, Taiwan, and the international GNSS Service community is appreciated. We thank the editor Jean-Phillippe Avouac, and two reviewers Kristel Chanard and Stacy Laroche for their detailed and constructive comments. We also thank H. Kao and C.-F. Ni for helpful discussions. This research is supported by the Institute of Earth Sciences, Academia Sinica, IESAS 2381, AS-CDA-105-M05 and the Ministry of Science and Technology, Taiwan grant MOST 108-2116-M-001-021-MY3. RB and YF acknowledge support by awards NNX17AE01G and 80NSSC19K0361 from the NASA Earth Surface and Interior program.

## Appendix A. Supplementary material

Supplementary material related to this article can be found online at <https://doi.org/10.1016/j.epsl.2020.116532>.

## References

- Altamimi, Z., Collilieux, X., Metivier, L., 2011. ITRF2008: an improved solution of the international terrestrial reference frame. *J. Geod.* 85, 457–473. <https://doi.org/10.1007/s00190-011-0444-4>.
- Argus, D.F., Fu, Y.N., Landerer, F.W., 2014. Seasonal variation in total water storage in California inferred from GPS observations of vertical land motion. *Geophys. Res. Lett.* 41, 1971–1980. <https://doi.org/10.1002/2014GL059570>.
- Argus, D.F., Landerer, F.W., Wiese, D.N., Martens, H.R., Fu, Y., Famiglietti, J.S., Thomas, B.F., Farr, T.G., Moore, A.W., Watkins, M.M., 2017. Sustained water loss in California's mountain ranges during severe drought from 2012 to 2015 inferred from GPS. *J. Geophys. Res., Solid Earth* 122, 10,559–10,585. <https://doi.org/10.1002/2017JB014424>.

- Bevis, M., Alsdorf, D., Kendrick, E., Fortes, L.P., Forsberg, B., Smalley Jr, R., Becker, J.J.G.R.L., 2005. Seasonal fluctuations in the mass of the Amazon River system and Earth's elastic response. *Geophys. Res. Lett.* 32. <https://doi.org/10.1029/2005GL023491>.
- Borsa, A.A., Agnew, D.C., Cayan, D.R., 2014. Ongoing drought-induced uplift in the western United States. *Science* 345, 1587–1590. <https://doi.org/10.1126/science.1260279>.
- Chaussard, E., Bürgmann, R., Shirzaei, M., Fielding, E., Baker, B., 2014. Predictability of hydraulic head changes and characterization of aquifer-system and fault properties from InSAR-derived ground deformation. *J. Geophys. Res., Solid Earth* 119, 6572–6590. <https://doi.org/10.1002/2014JB011266>.
- Chen, C.S., Chen, Y.L., 2003. The rainfall characteristics of Taiwan. *Mon. Weather Rev.* 131, 1323–1341. [https://doi.org/10.1175/1520-0493\(2003\)131<1323:TRCOT>2.0.CO;2](https://doi.org/10.1175/1520-0493(2003)131<1323:TRCOT>2.0.CO;2).
- Chen, C.-S., Chen, Y.-L., Liu, C.-L., Lin, P.-L., Chen, W.-C., 2007. Statistics of heavy rainfall occurrences in Taiwan. *Weather Forecast.* 22, 981–1002. <https://doi.org/10.1175/WAF1033.1>.
- Chen, C.S., Huang, J.M., 1999. A numerical study of precipitation characteristics over Taiwan island during the winter season. *Meteorol. Atmos. Phys.* 70, 167–183. <https://doi.org/10.1007/s007030050032>.
- Chen, G.T.-J., 1992. Mesoscale features observed in the Taiwan Mei-Yu season. *J. Meteorol. Soc. Jpn.* 70, 497–516. [https://doi.org/10.2151/jmsj1965.70.1B\\_497](https://doi.org/10.2151/jmsj1965.70.1B_497).
- Chen, J., Wilson, C., Tapley, B., Save, H., Cretaux, J.F., 2017. Long-term and seasonal Caspian Sea level change from satellite gravity and altimeter measurements. *J. Geophys. Res., Solid Earth* 122, 2274–2290. <https://doi.org/10.1002/2016JB013595>.
- Chen, K.H., Hwang, C., Chang, L.C., Ke, C.C., 2018. Short-time geodetic determination of aquifer storage coefficient in Taiwan. *J. Geophys. Res., Solid Earth* 123, 10,987–911,015. <https://doi.org/10.1029/2018JB016630>.
- Cheng, J., Lin, L., Lu, H., 2002. Influences of forests on water flows from headwater watersheds in Taiwan. *For. Ecol. Manag.* 165, 11–28. [https://doi.org/10.1016/S0378-1127\(01\)00626-0](https://doi.org/10.1016/S0378-1127(01)00626-0).
- Davis, J., Elósegui, P., Mitrovica, J., Tamisiea, M., 2004. Climate-driven deformation of the solid Earth from GRACE and GPS. *Geophys. Res. Lett.* 31. <https://doi.org/10.1029/2004GL021435>.
- Dill, R., 2008. Hydrological model LSDM for operational Earth rotation and gravity field variations, GFZ.
- Dill, R., Dobszlaw, H., 2013. Numerical simulations of global-scale high-resolution hydrological crustal deformations. *J. Geophys. Res., Solid Earth* 118, 5008–5017. <https://doi.org/10.1002/jgrb.50353>.
- Dong, D., Fang, P., Bock, Y., Webb, F., Prawirodirdjo, L., Kedar, S., Jamason, P., 2006. Spatiotemporal filtering using principal component analysis and Karhunen-Loeve expansion approaches for regional GPS network analysis. *J. Geophys. Res., Solid Earth* 111. <https://doi.org/10.1029/2005JB003806>.
- Dziewonski, A.M., Anderson, D.L., 1981. Preliminary reference Earth model. *Phys. Earth Planet. Inter.* 25, 297–356.
- Enzinger, T.L., Small, E.E., Borsa, A.A., 2018. Accuracy of snow water equivalent estimated from GPS vertical displacements: a synthetic loading case study for western US mountains. *Water Resour. Res.* 54, 581–599. <https://doi.org/10.1002/2017WR021521>.
- Farrell, W., 1972. Deformation of the Earth by surface loads. *Rev. Geophys.* 10, 761–797. <https://doi.org/10.1029/RG010i003p00761>.
- Fu, Y., Freymueller, J.T., 2012. Seasonal and long-term vertical deformation in the Nepal Himalaya constrained by GPS and GRACE measurements. *J. Geophys. Res., Solid Earth* 117. <https://doi.org/10.1029/2011JB008925>.
- Fu, Y.N., Argus, D.F., Landerer, F.W., 2015. GPS as an independent measurement to estimate terrestrial water storage variations in Washington and Oregon. *J. Geophys. Res.* 120, 552–566. <https://doi.org/10.1002/2014JB011415>.
- Gualandi, A., Serpelloni, E., Belardinelli, M., 2016. Blind source separation problem in GPS time series. *J. Geod.* 90, 323–341. <https://doi.org/10.1007/s00190-015-0875-4>.
- Hagemann, S., Dümenil, L., 1997. A parametrization of the lateral waterflow for the global scale. *Clim. Dyn.* 14, 17–31. <https://doi.org/10.1007/s003820050205>.
- Hagemann, S., Gates, L.D., 2003. Improving a subgrid runoff parameterization scheme for climate models by the use of high resolution data derived from satellite observations. *Clim. Dyn.* 21, 349–359. <https://doi.org/10.1007/s00382-003-0349-x>.
- Harris, R.A., Segall, P., 1987. Detection of a locked zone at depth on the Parkfield, California, segment of the San-Andreas Fault. *J. Geophys. Res.* 92, 7945–7962. <https://doi.org/10.1029/JB092iB08p07945>.
- Herring, T.A., King, R.W., McClusky, S.C., 2002. Documentation for the GAMIT Analysis Software, release 10.0 ed. Massachusetts Institute of Technology, Cambridge, MA.
- Hsu, S.K., 1998. Plan for a groundwater monitoring network in Taiwan. *Hydrogeol. J.* 6, 405–415. <https://doi.org/10.1007/s100400050163>.
- Hsu, Y.-J., Yu, S.-B., Simons, M., Kuo, L.-C., Chen, H.-Y., 2009. Interseismic crustal deformation in the Taiwan plate boundary zone revealed by GPS observations, seismicity, and earthquake focal mechanisms. *Tectonophysics* 479, 4–18. <https://doi.org/10.1016/j.tecto.2008.11.016>.
- Hsu, Y.-J., Chen, R.-F., Lin, C.-W., Chen, H.-Y., Yu, S.-B., 2014. Seasonal, long-term, and short-term deformation in the Central Range of Taiwan induced by landslides. *Geology* 42, 991–994. <https://doi.org/10.1130/G35991.1>.
- Hsu, Y.-J., Lai, Y.-R., You, R.-J., Chen, H.-Y., Teng, L.S., Tsai, Y.-C., Tang, C.-H., Su, H.-H., 2018. Detecting rock uplift across southern Taiwan mountain belt by integrated GPS and leveling data. *Tectonophysics* 744, 275–284.
- Hyvärinen, A., Oja, E., 2000. Independent component analysis: algorithms and applications. *Neural Netw.* 13, 411–430. [https://doi.org/10.1016/S0893-6080\(00\)00026-5](https://doi.org/10.1016/S0893-6080(00)00026-5).
- Johnson, C.W., Fu, Y., Bürgmann, R., 2017. Seasonal water storage, stress modulation, and California seismicity. *Science* 356, 1161–1164. <https://doi.org/10.1126/science.aak9547>.
- Kuhlman, K.L., Hinnell, A.C., Mishra, P.K., Yeh, T.C.J., 2008. Basin-scale transmissivity and storativity estimation using hydraulic tomography. *Groundwater* 46, 706–715. <https://doi.org/10.1111/j.1745-6584.2008.00455.x>.
- Kusche, J., Schrama, E., 2005. Surface mass redistribution inversion from global GPS deformation and Gravity Recovery and Climate Experiment (GRACE) gravity data. *J. Geophys. Res., Solid Earth* 110. <https://doi.org/10.1029/2004JB003556>.
- Lee, C.-H., Chen, W.-P., Lee, R.-H., 2006. Estimation of groundwater recharge using water balance coupled with base-flow-record estimation and stable-base-flow analysis. *Environ. Geol.* 51, 73–82. <https://doi.org/10.1007/s00254-006-0305-2>.
- Lee, J.C., Angelier, J., Chu, H.T., Hu, J.C., Jeng, F.S., Rau, R.J., 2003. Active fault creep variations at Chihshang, Taiwan, revealed by creep meter monitoring, 1998–2001. *J. Geophys. Res.* 108. <https://doi.org/10.1029/2003JB002394>.
- Milliner, C., Materna, K., Bürgmann, R., Fu, Y., Moore, A.W., Bekaert, D., Adhikari, S., Argus, D.F., 2018. Tracking the weight of Hurricane Harvey's stormwater using GPS data. *Sci. Adv.* 4, eaau2477. <https://doi.org/10.1126/sciadv.aau2477>.
- Rodell, M., Houser, P., Jambor, U., Gottschalk, J., Mitchell, K., Meng, C.-J., Arsenault, K., Cosgrove, B., Radakovich, J., Bosilovich, M., 2004. The global land data assimilation system. *Bull. Am. Meteorol. Soc.* 85, 381–394. <https://doi.org/10.1175/BAMS-85-3-381>.
- Sun, Y., Riva, R., Ditmar, P., 2016. Optimizing estimates of annual variations and trends in geocenter motion and J<sub>2</sub> from a combination of GRACE data and geophysical models. *J. Geophys. Res.* 121, 8352–8370. <https://doi.org/10.1002/2016JB013073>.
- Swenson, S., Chambers, D., Wahr, J., 2008. Estimating geocenter variations from a combination of GRACE and ocean model output. *J. Geophys. Res., Solid Earth* 113. <https://doi.org/10.1029/2007JB005338>.
- Tapley, B.D., Bettadpur, S., Ries, J.C., Thompson, P.F., Watkins, M.M., 2004. GRACE measurements of mass variability in the Earth system. *Science* 305, 503–505. <https://doi.org/10.1126/science.1099192>.
- Ting, C.-S., Kerh, T., Liao, C.-J., 1998. Estimation of groundwater recharge using the chloride mass-balance method, Pingtung Plain, Taiwan. *Hydrogeol. J.* 6, 282–292. <https://doi.org/10.1007/s100400050151>.
- Wahr, J., Molenaar, M., Bryan, F., 1998. Time variability of the Earth's gravity field: hydrological and oceanic effects and their possible detection using GRACE. *J. Geophys. Res.* 103, 30205–30229.
- Wahr, J., Swenson, S., Zlotnicki, V., Velicogna, I., 2004. Time-variable gravity from GRACE: first results. *Geophys. Res. Lett.* 31. <https://doi.org/10.1029/2004GL019779>.
- Wang, C.-H., Li, L.-A., Liu, W.-C., 1994. Some characteristics of the precipitation in Taiwan. In: *Biodiversity and Terrestrial Ecosystem*, pp. 343–354.
- Wang, H.S., Xiang, L.W., Jia, L.L., Jiang, L.M., Wang, Z.Y., Hu, B., Gao, P., 2012. Load love numbers and Green's functions for elastic Earth models PREM, iasp91, ak135, and modified models with refined crustal structure from Crust 2.0. *Comput. Geosci.* 49, 190–199. <https://doi.org/10.1016/j.cageo.2012.06.022>.
- Water Resources Agency, Ministry of Economic Affairs, 2002. Integration project on groundwater monitoring and land subsidence prevention.
- Watkins, M.M., Wiese, D.N., Yuan, D.-N., Boening, C., Landerer, F.W., 2015. Improved methods for observing Earth's time variable mass distribution with GRACE using spherical cap mascons. *J. Geophys. Res.* 120, 2648–2671. <https://doi.org/10.1002/2014JB011547>.
- Yu, S.-B., Chen, H.-Y., Kuo, L.C., 1997. Velocity field of GPS stations in the Taiwan area. *Tectonophysics* 274, 41–59.